



Cite as
Nano-Micro Lett.
(2024) 16:114

Received: 7 September 2023
Accepted: 11 December 2023
© The Author(s) 2024

Janus Quasi-Solid Electrolyte Membranes with Asymmetric Porous Structure for High-Performance Lithium-Metal Batteries

Zerui Chen¹, Wei Zhao¹, Qian Liu¹, Yifei Xu¹, Qinghe Wang¹, Jinmin Lin¹, Hao Bin Wu¹ ✉

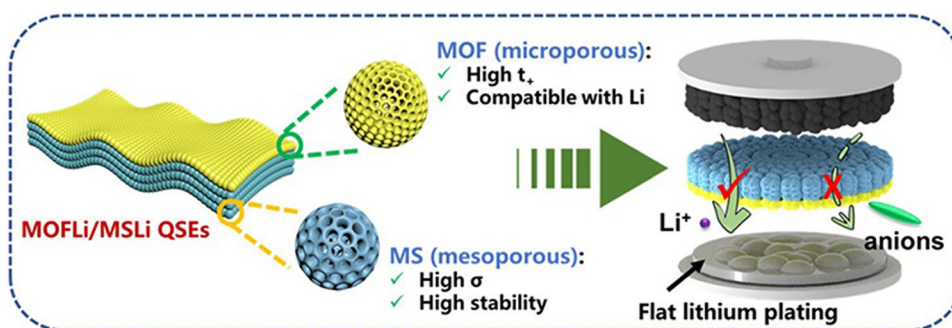
HIGHLIGHTS

- Janus quasi-solid electrolyte membranes with asymmetric porous structure were constructed, showing a high σ_{Li^+} of $1.5 \times 10^{-4} \text{ S cm}^{-1}$ and a high t_+ of 0.71.
- The solvation structures and ion transport dynamics in nanopores have been deciphered, manifesting a concentrated electrolyte-like structure and regulated transport behaviors.
- Quasi-solid NCM 622//Li cells have been demonstrated to stably cycle for 200 cycles at 1 C, and pouch cell has shown high tolerance for abuse.

ABSTRACT Quasi-solid electrolytes (QSEs) based on nanoporous materials are promising candidates to construct high-performance Li-metal batteries (LMBs). However, simultaneously boosting the ionic conductivity (σ) and lithium-ion transference number (t_+) of liquid electrolyte confined in porous matrix remains challenging.

Herein, we report a novel Janus MOFLi/MSLi QSEs with asymmetric porous structure to inherit the benefits of both mesoporous and microporous hosts. This Janus QSE composed of mesoporous silica and microporous MOF exhibits a neat Li^+ conductivity of $1.5 \times 10^{-4} \text{ S cm}^{-1}$ with t_+ of 0.71. A partially de-solvated structure and preference distribution of Li^+ near the Lewis base O atoms were depicted by MD simulations. Meanwhile, the nanoporous structure enabled efficient ion flux regulation, promoting the homogenous deposition of Li^+ . When incorporated in Li//Cu cells, the MOFLi/MSLi QSEs demonstrated a high Coulombic efficiency of 98.1%, surpassing that of liquid electrolytes (96.3%). Additionally, NCM 622//Li batteries equipped with MOFLi/MSLi QSEs exhibited promising rate performance and could operate stably for over 200 cycles at 1 C. These results highlight the potential of Janus MOFLi/MSLi QSEs as promising candidates for next-generation LMBs.

KEYWORDS Metal–organic frameworks; Mesoporous silicas; Quasi-solid electrolytes; Janus structure; Lithium-metal battery



✉ Hao Bin Wu, hbwu@zju.edu.cn

¹ Institute for Composites Science Innovation (InCSI) and State Key Laboratory of Silicon and Advanced Semiconductor Materials, School of Materials Science and Engineering, Zhejiang University, Hangzhou 310027, People's Republic of China

1 Introduction

Nanoporous materials, exemplified by metal–organic frameworks (MOFs) [1, 2], covalent-organic frameworks (COFs) [3–5], and zeolites [6], have unique structural properties, including high surface area, tunable pore size, and adjustable chemical properties. These features enable them to construct quasi-solid electrolytes (QSEs) for next-generation rechargeable batteries such as Li-metal batteries (LMBs) [7–13]. By confining liquid electrolytes in microporous or mesoporous channels, QSEs derived from nanoporous materials exhibit decent room-temperature ionic conductivity (σ) ($> 10^{-4}$ S cm^{-1}) [14]. Moreover, the porous hosts have been found to inhibit the migration of anions [15, 16] and tailor the solvation structure of Li^+ ions [17–19], resulting in high Li-ion transference number (t_+) (typically exceeding 0.6) and enhanced stability. These features warrant QSEs as promising electrolyte candidates toward safe and durable LMBs.

Critical determinants of the cycling performance of Li-metal anode (LMA), as governed by Sand's law [20], are the ionic conductivity and transference number of Li^+ ions in electrolytes. Previous works have investigated the effects of pore structure [21], pore size [8, 22], and charge of the inner surface [8, 23] on ionic conductivity, concluding that larger pore size generally facilitates the migration of Li^+ . However, it is difficult to achieve both high σ and t_+ when confining liquid electrolytes in a single type of porous material, as larger pore size weakens the confinement of liquid components and the ability to inhibit anion migration, compromising the advantages of QSEs. Additionally, though previous investigations have indicated the tailored solvation structure of Li^+ ions in the nanopores [19], a clear depiction of the electrolyte structure at the atom level is still absent [24], impeding a comprehensive understanding of Li^+ migration behavior.

To achieve balanced σ and t_+ in QSEs, we proposed novel Janus QSE membranes with asymmetric porous structure (denoted as MOFLi/MSLi QSEs) (Scheme 1). The primary layer was constructed using mesoporous silica (MS) nanoparticles, which allow the uptake of large quantity of liquid electrolyte and fast ionic transport in the mesopores [25]. Meanwhile, the MS is light weighted and chemically stable [26], which are helpful to improve the energy density and safety of LMBs. The second layer with a much thinner thickness was composed of metal–organic framework (MOF) nanoparticles with a microporous structure to regulate the

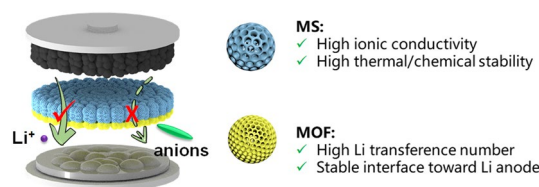
solvation structure of electrolyte. UiO-66, a specific Zr-based MOF, was selected for its easy synthesis [27], ability to improve t_+ [28], and excellent interfacial compatibility of the derived QSE for LMA [29]. Such asymmetric porous structure design overcomes the trade-off between σ and t_+ , and the resulting MOFLi/MSLi QSE displays a neat Li^+ ion conductivity (σ_{Li^+}) up to 1.5×10^{-4} S cm^{-1} and high t_+ of 0.71. The solvation structure of Li^+ in MOF and MS was investigated by molecular dynamic (MD) simulation, depicting a desolvation structure and the preferred distribution of Li^+ near the Lewis base O atoms of the porous hosts. Additionally, the nanoporous channels of MOFLi/MSLi QSEs effectively regulated ion flux and inhibited the growth of Li dendrites. LillLi cells with MOFLi/MSLi QSEs demonstrated an extended cycling life, suggesting improved interfacial stability with LMA. NCM 622||Li batteries equipped with MOFLi/MSLi QSEs showed excellent rate performance and can stably work for 200 cycles at 1C. We further demonstrated a pouch cells (5.15 cm \times 4.2 cm) with a total cathode capacity of 32.7 mA h, which could operate safely even under blending and cutting.

2 Experimental Section

2.1 Synthesis of MOF and MS Particles

2.1.1 Synthesis of UiO-66 nanoparticles

UiO-66 nanoparticles were synthesized according to our previous work [29]. Briefly, ZrCl_4 (0.28 g, 1.372 mmol), H_2BDC (0.20 g, 1.372 mmol), and 10 equivalents of benzoic acid (HBC) were dissolved in 70 mL DMF in a Teflon liner by stirring for about 30 min. The Teflon liner was then sealed in an autoclave and heated in an oven at 120 °C for 24 h. After cooling to room temperature, the



Scheme 1 Schematic illustration of the Janus MSLi/MOFLi QSEs with an asymmetric porous structure

solids were isolated by centrifugation, followed by being washed with DMF and ethanol several times, and then dried at 70 °C. The solids were further treated with 1 M HCl solution for 30 min to remove the coordinated HBC. The acid-treated solids were washed with deionized water, DMF, and ethanol and then dried under vacuum at 250 °C for 4 h to obtain activated UiO-66 nanoparticles.

2.1.2 Synthesis of MS nanoparticles

Mesoporous silica (MS) nanoparticles were synthesized following the method reported by Wang et al. [30]. Briefly, deionized water (20 mL) and ethanol (5 mL) were mixed to get a homogeneous solution. Then, 50 mg of triethanolamine and 0.2 g of cetyltriethylammonium bromide were added into the above solution and stirred at 60 °C for 30 min. Subsequently, 2 mL of tetraethyl orthosilicate was added and stirred at 60 °C for another 2 h. 20 mL of ethanol was added into the white solution and cooled down to ambient temperature. The precipitate was collected by centrifugation and then washed with deionized water and ethanol several times. After being dried at 70 °C overnight, the powders were calcined at 550 °C for 5 h to get MS.

2.2 Preparation of Quasi-solid Electrolytes

2.2.1 Preparing of MOFLi or MSLi QSE Pellets

MOF or MS (100 mg) and PVDF-HFP (100 mg) were mixed in dimethoxyethane (DME) to form a homogeneous solution and then dried at 50 °C under a vacuum. The solid product was pressed into a pellet with a diameter of 10 mm under a pressure of 10 MPa. The pellet was immersed in 1 M LiTFSI in polycarbonate (PC) solution for 4 h, and the QSE pellets were obtained.

2.2.2 Preparation of MOFLi or MSLi QSE membranes

MOF or MS (400 mg), glass fiber (20 mg), PVDF (100 mg), and LiTFSI (57 mg) were mixed in NMP (2.5 mL) to form a homogeneous gel. The gel was cast onto a cleaned glass plate. The casting gap of 100 µm was used for casting the membrane. Then, the gel was dried at 80 °C under

a vacuum overnight to produce a free-standing membrane. The membrane was pouched into disks with a diameter of 18 mm and further dried at 120 °C for 10 h. Liquid electrolyte was then added based on the mass ratio (MOF or MS: LEs = 5: 4) obtained from QSE pellets.

2.2.3 Preparation of Janus MOFLi/MSLi QSE membrane

MS membrane was first prepared on a cleaned glass plate following the above procedure. To introduce the MOF layer, a homogeneous gel containing 100 mg of MOF, 25 mg of PVDF-HFP, and 1.25 mL of DME was prepared. The gel was then casted on the above MS membrane with a casting gap of 75 µm. After simply drying at ambient temperature, a free-standing membrane was harvested. The membrane was pouched into disks with a diameter of 18 mm and further dried at 120 °C for 10 h. Liquid electrolyte was then added based on the mass ratio MOF/MS: LEs = 6: 4.

3 Result and Discussion

3.1 Design Principle and Structural Characterizations

MOF and MS particles were synthesized following previously reported methods [29, 30] and characterized by scanning electron microscopy (SEM) and powder X-ray diffraction (PXRD). SEM images demonstrated that both MOF and MS particles displayed uniform spherical morphology with diameters of about 80 nm (Fig. 1a, b). PXRD patterns indicated that the MOF particles possessed a crystal structure of UiO-66 [31] while MS particles were amorphous (Fig. 1c). Both the MOF and MS particles exhibited remarkable thermal stability as illustrated in Fig. S1. The observed mass loss below 300 °C can be attributed to the release of absorbed moisture [32–34]. Notably, the MOF particles start to decompose at approximately 500 °C, while the MS particles exhibited excellent thermal stability up to 700 °C. The pore structures of MOF and MS particles were then explored by nitrogen adsorption–desorption measurements (Figs. 1d, S2 and Table S1) [35]. The MOF particles displayed two kinds of pore configurations [36] with pore diameters of 0.6 and 1.2 nm, respectively, showing a pore volume of 0.62 cm³ g⁻¹. The MS particles were mesoporous with a pore diameter of 12 nm and a pore volume of 0.76 cm³ g⁻¹.

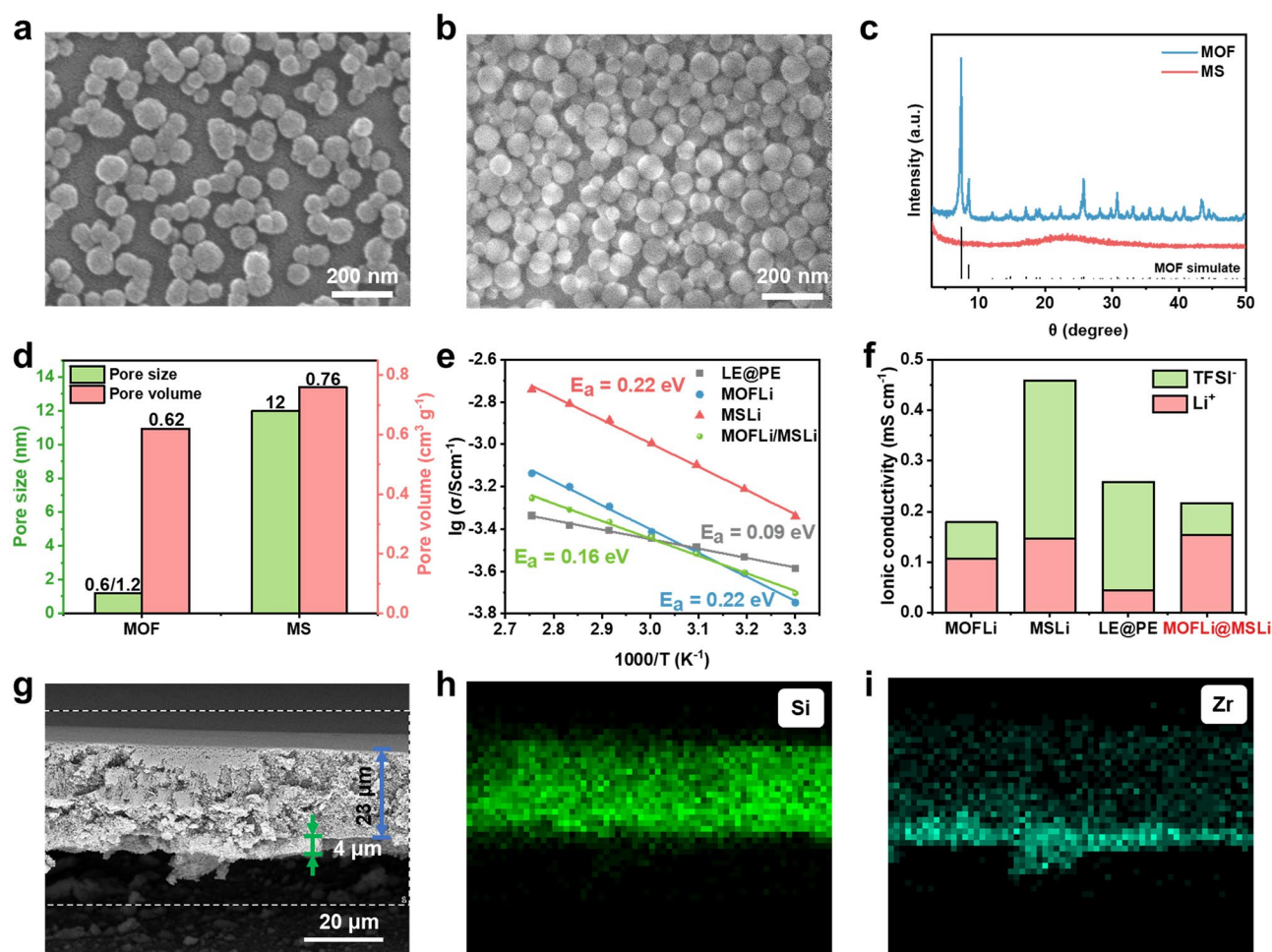


Fig. 1 Structure characterization and electrochemical properties of MOF and MS particles. **a** SEM image of MOF particles and **b** MS particles. **c** PXRD patterns of the as-synthesized MOF and MS particles. **d** Pore size and pore volume of MOF and MS. **e** Corresponding Arrhenius plots of the ionic conductivity of LE in PE membrane (LE@PE, MOFLi QSEs, MSLi QSEs and MOFLi/MSLi QSEs). **f** Ionic conductivity corresponding to Li^+ and TFSI^- of different samples based on EIS plots and t_+ measurement. **g-i** SEM image and corresponding energy dispersive spectrometry (EDS) mapping of Janus MOF/MS membrane

The MS with low tap density (Fig. S3) minimizes the extra weight brought by electrolytes, which is advantageous when comparing with inorganic solid electrolytes of high density.

In order to obtain QSEs, MOF and MS powers were firstly compressed into pellets with 20 wt% PVDF-HFP (functioned as binder). The obtained MOF@PVDF-HFP and MS@PVDF-HFP displayed a slight decrease in pore size and pore volume (Fig. S2 and Table S1), but still exhibited microporous and mesoporous structures, respectively. The pellets were subsequently soaked in 1 M LiTFSI in PC solution. After fully adsorbed with liquid electrolytes, QSE pellets were harvested (denoted as MOFLi QSE and MSLi QSE). Benefiting from the larger pore size and pore

volume, MSLi QSEs were able to adsorb more liquid electrolyte (39 wt%) than MOFLi QSEs (23 wt%) (Fig. S4). The ionic conductivities of MOFLi QSEs and MSLi QSEs were investigated using electrochemical impedance spectroscopy (EIS) (Figs. 1e and S5). MOFLi QSE and MSLi QSE displayed room-temperature ionic conductivity (σ_{total}) of about 1.6×10^{-4} and 4.6×10^{-4} S cm^{-1} , respectively. Additionally, PVDF-HFP-based gel electrolyte exhibited room-temperature ionic conductivity of only 1.6×10^{-5} S cm^{-1} (Fig. S6), which contributed little to the ionic conductivity of QSE. Though the pure liquid electrolyte (LE) (1 M LiTFSI in PC) demonstrated σ_{total} up to 5.6×10^{-3} S cm^{-1} , liquid electrolyte in commercial PE membrane only delivered σ_{total} of

$2.6 \times 10^{-4} \text{ S cm}^{-1}$. Both the MS and MOF surfaces of the QSE exhibit remarkable wettability with liquid electrolyte as confirmed by the contact angle measurement (Fig. S7) [37]. The contact angles of LE on MS and MOF membranes are notably smaller than that on PE membrane (18.7° and 23.5° vs. 71.6°). Porosity of the MOF and MS pellets estimated by the LE uptakes is 28% and 49%, respectively, while that of PE membrane is 35% (Table S2). The high LE uptake of MS membrane and its excellent wettability with LE explain the higher ionic conductivity of MSLi QSE compared with LE in PE membrane.

Lithium-ion transference number (t_+) was further measured to assess the contributions of Li^+ and TFSI^- ions to total ionic conductivity (Figs. 1f and S8). Benefiting from the microporous structure and strong MOF-LE interaction, MOFLi QSE is capable to restrict the migration of anions and delivered t_+ up to 0.60, while MSLi QSE and liquid electrolyte in PE membrane could only offer t_+ of 0.32 and 0.17, respectively. With both σ_{total} and t_+ taken into consideration, MSLi QSE displays the highest neat Li^+ conductivity (σ_{Li^+}) of $1.5 \times 10^{-4} \text{ S cm}^{-1}$ while MOFLi QSE demonstrates the lowest TFSI^- conductivity (σ_{TFSI^-}) of $7.2 \times 10^{-5} \text{ S cm}^{-1}$.

To develop QSEs with convenient Li^+ migration and restrained TFSI^- transport, Janus QSEs with asymmetric porous structure were proposed by applying MS as the major layer to conduct Li^+ and MOF as the functional layer to hinder TFSI^- migration. The Janus MOF/MS membrane was fabricated using a layer-by-layer tape casting method (see Experimental section and Fig. S9), which enables large-area fabrication of the Janus membrane (Fig. S10). The Janus membrane consists of a relatively thick MS layer to ensure high ionic conductivity and a relatively thin MOF layer to inhibit the migration of anions [10, 38]. As demonstrated in Fig. 1g-i, MOF/MS membrane finally delivered asymmetric double-layer structure with a total thickness of about $27 \mu\text{m}$, of which the MS layer was $23 \mu\text{m}$ and the MOF layer was $4 \mu\text{m}$. The MOF/MS membrane is dense, and the upper surface of the membrane (MOF side) exposed to air during drying was relatively rough (Fig. S11). High thermal stability of MOF and MS enabled the MOF/MS membrane to maintain the original structure up to 200°C , while commercial PE membrane suffered from dramatic shrink (Fig. S12). Meanwhile, the Yang's modulus of the MOFLi/MSLi membrane was examined using atomic force microscopy (AFM) as shown in Fig. S13. The average Yang's moduli on MSLi and MOFLi sides are 1.66 and 1.43 GPa, respectively, which are

notably higher than that of PE membrane (160 MPa). The Janus structure enabled MOFLi/MSLi QSE to deliver σ_{total} of $2.2 \times 10^{-4} \text{ S cm}^{-1}$ and t_+ up to 0.71, translating to σ_{Li^+} of $1.5 \times 10^{-4} \text{ S cm}^{-1}$, which was comparable with that of MSLi QSEs. The simultaneously displayed high Li^+ ion conductivity and low TFSI^- ion conductivity suggested the efficient asymmetric structure design of MOFLi/MSLi QSEs.

3.2 Solvation Structure and Ion Transport Dynamic

The solvation structure and ion transport dynamics of QSEs were analyzed by molecular dynamic (MD) simulations [39]. Three models, namely MOFLi, MSLi, and LEs, were set up for MD simulations (Fig. 2a-c). The change in the solvation structure of Li^+ ions in different electrolytes was revealed by radial distribution function (RDF) (Fig. 2d-f). In LE, Li^+ was fully solvated by PC molecules, with an average coordination number (CN) of 4.4. When confined in porous hosts, due to the spatial restriction of pore size, a de-solvation process took place on Li^+ ions to generate a smaller solvation sheath, reflected by the reduction of CN of O(PC) (3.8 and 1.9 for MSLi and MOFLi, respectively). Moreover, the Lewis base atoms of the porous hosts (O(Zr-O-C) from MOF and O(Si-O-Si) from MS) seem to participate in the solvation of Li^+ (Fig. S14), delivering coordination number of 2.7 and 1.3, respectively. Such interaction between porous hosts and Li^+ ions results in preferential location of Li^+ ions near the O atoms in the pore wall [40–42], contrasting with their homogeneous distribution in LE (Figs. 2a-c and S15). Additionally, TFSI^- competed to enter the solvation sheath of Li^+ due to the decrease in CN of PC, reflected by the increase in the ratio of $g(r)$ attributed to O(TFSI^-) and O(PC) (Fig. S16). The change in the solvation structure of Li^+ leads to different migration mechanism [24], which is evidenced by the change in activation energy in Arrhenius plots (0.22, 0.22, and 0.09 eV for MOFLi QSE, MSLi QSE, and LE in PE membrane, respectively) (Fig. 1d).

Furthermore, to confirm the unique solvation structures of QSEs obtained by MD simulations, Raman spectra were performed on different electrolytes (Figs. 2g-i and S17). Peaks at around $700\text{--}780 \text{ cm}^{-1}$ were attributed to the vibrations of TFSI^- anions, which are affected by the solvation with Li^+ ions [7, 17, 43]. Peaks at 722 cm^{-1} were assigned to solvent-separate ion pairs (SSIP) while peaks

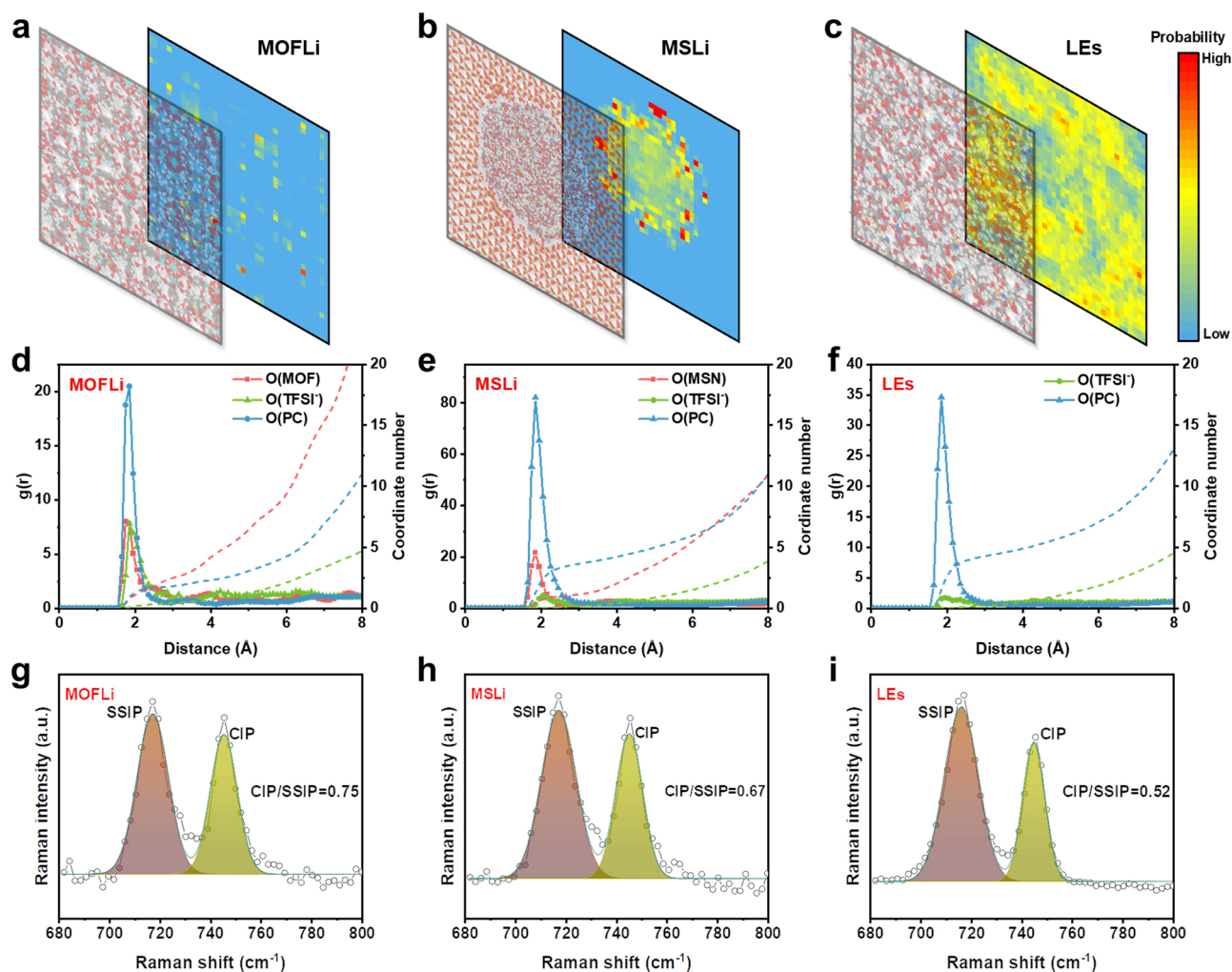


Fig. 2 Molecular dynamic (MD) simulations of different electrolytes. The final snap of the models and the distribution of Li^+ during the whole simulation procedure of **a** MOFLi, **b** MSLi, and **c** LEs. Radial distribution function (RDF) and Raman spectra of **d**, **g** MOFLi, **e**, **h** MSLi and **f**, **i** LEs

at 746 cm^{-1} were attributed to the formation of contact ion pairs (CIP) with Li^+ ions. Increasing the concentration of liquid electrolyte (from 0.3 to 3 M) leads to the enhanced intensity of CIP-peaks (Fig. S17), which reflects the change of solvation structure [7]. When liquid electrolyte was confined in the nanoporous host, the solvation sheath of Li^+ would be tailored and more TFSI $^-$ ions would coordinate with Li^+ ions to form CIPs. The higher ratio between CIPs and SSIPs in MOFLi and MSLi than 1 M LiTFSI/PC electrolyte revealed that a concentrated-electrolyte-like solvation structure is created in the nanopore channels, which is helpful to achieve an anion-induced SEI on LMA [19, 44]. The higher proportion of CIPs in

QSEs might partly explain the high t_+ due to the restricted migration of anions as well as the lower Li^+ conductivity compared with pure LE.

Mean squared displacement (MSD) reflects the diffusion ability of Li^+ and TFSI $^-$ in MOFLi QSE, MSLi QSE, and pure liquid electrolyte (LE) [40] (Fig. S18). The largest MSD value of Li^+ and TFSI $^-$ in LE indicated their highest mobility in pure liquid phase. When liquid electrolyte is confined in porous hosts, the diffusion of both Li^+ and TFSI $^-$ was restricted due to the restriction of the porous matrix and interaction with the Lewis base O atoms, yielding ionic diffusion coefficients (D_{diff}) in the order of $D_{\text{LE}} > D_{\text{MSLi}} > D_{\text{MOFLi}}$. Nonetheless, the diffusion of Li^+ and TFSI $^-$ was impeded by

porous hosts to different extents. When confined in microporous MOF particles, the migration of TFSI⁻ ions was tremendously restricted since the size of anions (about 0.8 nm) is close to the pore window size of the MOF particles. The trend in how the ion transport dynamics change in the porous hosts predicted by MD simulations is consistent with the experimental results, confirming the effective modulation of ion transport by specific porous hosts.

3.3 Ion Flux Regulation and Lithium Deposition

Apart from the high σ_{Li^+} and high t_+ by integrating the merits of mesoporous MS and microporous MOF, MOFLi/MSLi QSEs also inherit their advantage of ion flux regulation, which is also crucial for achieving homogeneous Li deposition and preventing the growth of Li dendrites. To investigate the effect of the pore structure on ion flux regulation, the finite element method (FEM) was used to simulate ion flux in different electrolytes [29, 45, 46] (Figs. 3a-c and S19). In the PE membrane with a large pore size, obvious ion flux turbulence with extremely high current density in certain areas was observed, which is hazardous for Li deposition since the concentration polarization is exacerbated and dendrites grow quickly. In contrast, the nanoporous structures of MSLi and MOFLi QSEs efficiently homogenize the ion flux distribution. The influence of local current density on the growth of Li dendrites was further simulated (Figs. 3d-f and S20). With the increase in current density, obvious Li protrusions formed on top of the electrode, which would gradually evolve into dendritic structures. The morphologies of the deposited Li on Cu collectors using various electrolytes corroborated with the FEM simulation results (Fig. 3g-i). PE membrane with liquid electrolyte was not capable to regulate ion flux but accelerated the growth of Li dendrites. In contrast, homogenous nanoporous channels, particularly the microporous channels in MOFLi QSE, favor the uniform and dense Li deposition, which would improve the efficiency and durability of LMA. Similar homogeneity in Li deposition can be achieved by MOFLi/MSLi QSE once the MOFLi layer is in close contact with LMA as discussed shortly.

3.4 Cycling Performance of LMBs

LillLi cells equipped with advantaged MOFLi/MSLi QSE membrane showed much extended cycling life than PE

membrane with 1 M LiTFSI in PC liquid electrolyte, confirming the ability of MOFLi/MSLi QSE to improve the performance of LMA (Fig. S21). To construct the full cells of LMB, QSE made with commercial liquid electrolyte (1 M LiPF₆ in EC/DMC (1:1 by volume) with 5% FEC) was further evaluated. LillCu cells were assembled to evaluate the Coulombic efficiency (CE) of Li deposition/stripping in different electrolytes (Fig. 4a). When equipped with MOFLi/MSLi QSE, a high average CE up to 98.1% was harvested, compared with the CE of 96.3% when using a PE membrane and liquid electrolyte. Furthermore, MOFLi/MSLi QSE yielded a lower nucleation potential of 72 mV compared with that of 120 mV in liquid electrolyte (Fig. S22), which might attribute to the affinity of the MOF layer toward Li⁺ [29]. As illustrated in Figs. 4b, c and S23, after electrochemically depositing 5 mAh cm⁻² of Li on bare Cu current collector, macroscopically uneven Li deposition was observed when using PE membrane and liquid electrolyte, compared with the flat surface harvested from the cell equipped with MOFLi/MSLi QSE. SEM images illustrated serious Li dendrite growth when using PE membrane. The homogenous Li deposition with columnar shape enabled by MOFLi/MSLi QSE could be attributed to the high σ_{Li^+} and t_+ , regulated ion flux, and reduced nucleation barrier.

Critical current density (CCD) of MOFLi/MSLi QSEs was assessed to evaluate the capability to operate at high current densities. As shown in Fig. S24, MOFLi and MSLi QSEs experienced a short circuit at current densities of 0.7 and 1.2 mA cm⁻², respectively. In contrast, Janus MOFLi/MSLi QSEs demonstrated high tolerance to increasing current densities up to 2.1 mA cm⁻². Lillthin Li (25 μm) cells were also assembled to evaluate the utilization of Li (Fig. 4d). Cells using MOFLi and MSLi QSEs suffered from quick failure, probably relating to the inefficient σ_{Li^+} or t_+ when operating under rigorous condition. In contrast, cell using MOFLi/MSLi QSE can stably work for 230 h with a low overpotential of 21 mV. X-ray photoelectron spectroscopy (XPS) was performed on the lithium anode after 10 cycles to investigate the composition of the SEI layer. As shown in Fig. S25, all samples exhibited C 1s peaks at 286.4, 288.7, and 289.8 eV, corresponding to C–O, C=O, and Li₂CO₃, respectively, which originated from the decomposition of carbonate solvent. The F 1s peaks at 684.8 and 686.6 eV were identified as signals of LiF and Li_xPO_xF_z, respectively, resulting from the decomposition of lithium salt [47–49]. Remarkably, the content of Li₂CO₃ is lower on

Li cycled with MOFLi/MSLi QSE compared to those with MOFLi and MSLi, which suggest less solvent decomposition. New peaks corresponding to C–F in the C 1s spectrum (291.2 eV) and F 1s spectrum (688.6 eV) might come from the decomposition of PVDF-HFP in the MOF layer.

The oxidation stability of MSLi and MOFLi QSEs was assessed through linear sweep voltammetry (LSV) measurements. As depicted in Fig. S26, MSLi QSE exhibited superior cathodic stability up to 4.6 V, surpassing the stability of MOFLi QSE (4.25 V). The exceptional oxidation stability of MSLi QSE enables the use of high-voltage cathode for high-energy LMBs. Herein, full cells of LMB using high-voltage cathode (NCM 622) were assembled. The full cell

equipped with MOFLi/MSLi QSE showed favorable rate performance, delivering a specific capacity of 168, 160, 147, 131, and 107 mAh g⁻¹ at 0.1, 0.2, 0.5, 1, 2, and 5 C, respectively (Fig. 4e, f). NCM 622||Li batteries (NCM 622 loading: 1.0 mg cm⁻²) could stably work for 200 cycles with 70% capacity retention (Fig. 4g), maintaining a CE of 99.5%. The Janus MOFLi/MSLi QSEs are also compatible with other high-energy cathodes such as LiCoO₂ (LCO). As shown in Fig. S27, LCO||Li batteries demonstrated excellent rate performance, delivering specific capacities of 143, 136, 124, 110, 92, and 77 mAh g⁻¹ at 0.1, 0.2, 0.5, 1, 2, and 3 C, respectively. LCO||Li batteries (LCO loading: 0.8 mg cm⁻²) also exhibited stable operation for 200 cycles with 83%

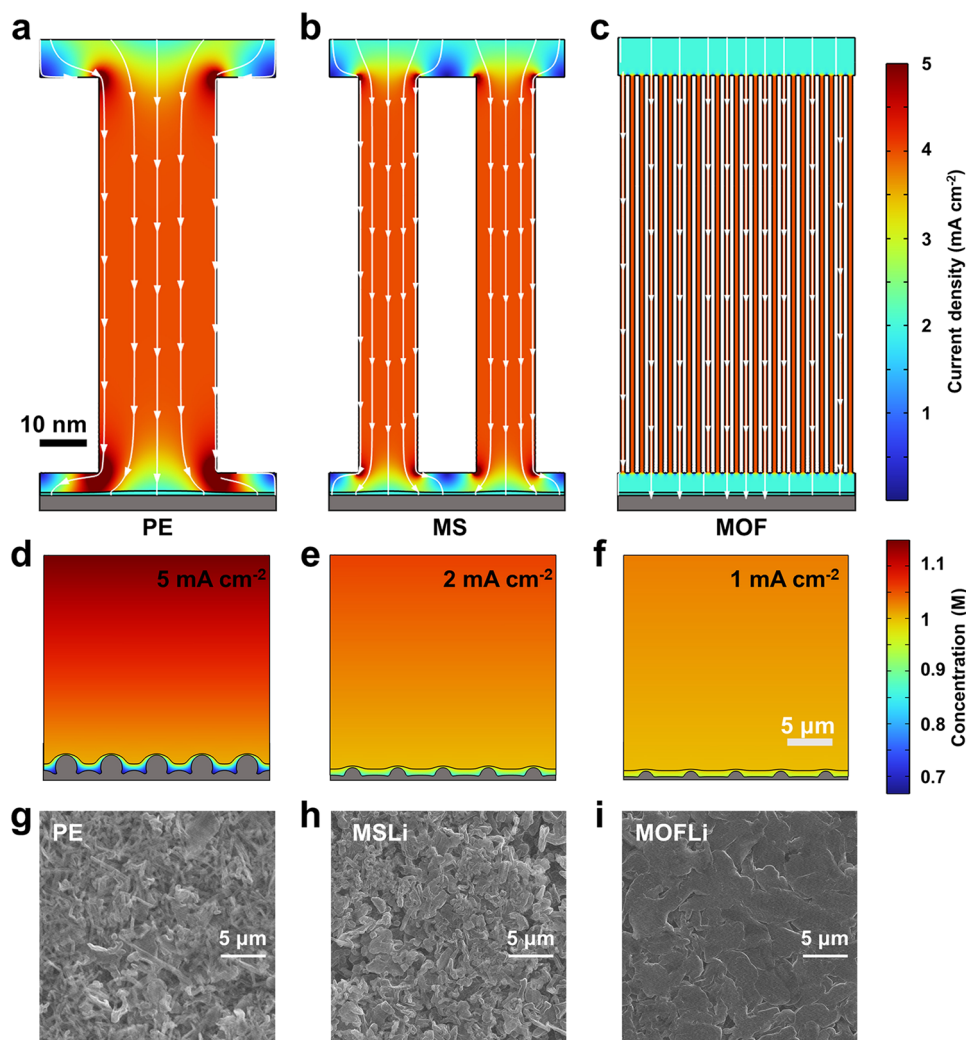


Fig. 3 Finite element method (FEM) simulations of different types of electrolytes. Ion flux distribution when employing **a** LEs in PE membrane, **b** MSLi QSEs and **c** MOFLi QSEs. Simulation of the deposition of Li⁺ at a local current density of **d** 5 mA cm⁻², **e** 2 mA cm⁻², and **f** 1 mA cm⁻². **g-i** The morphology of the deposited Li under a current density of 0.5 mA cm⁻² and a capacity of 5 mAh cm⁻²

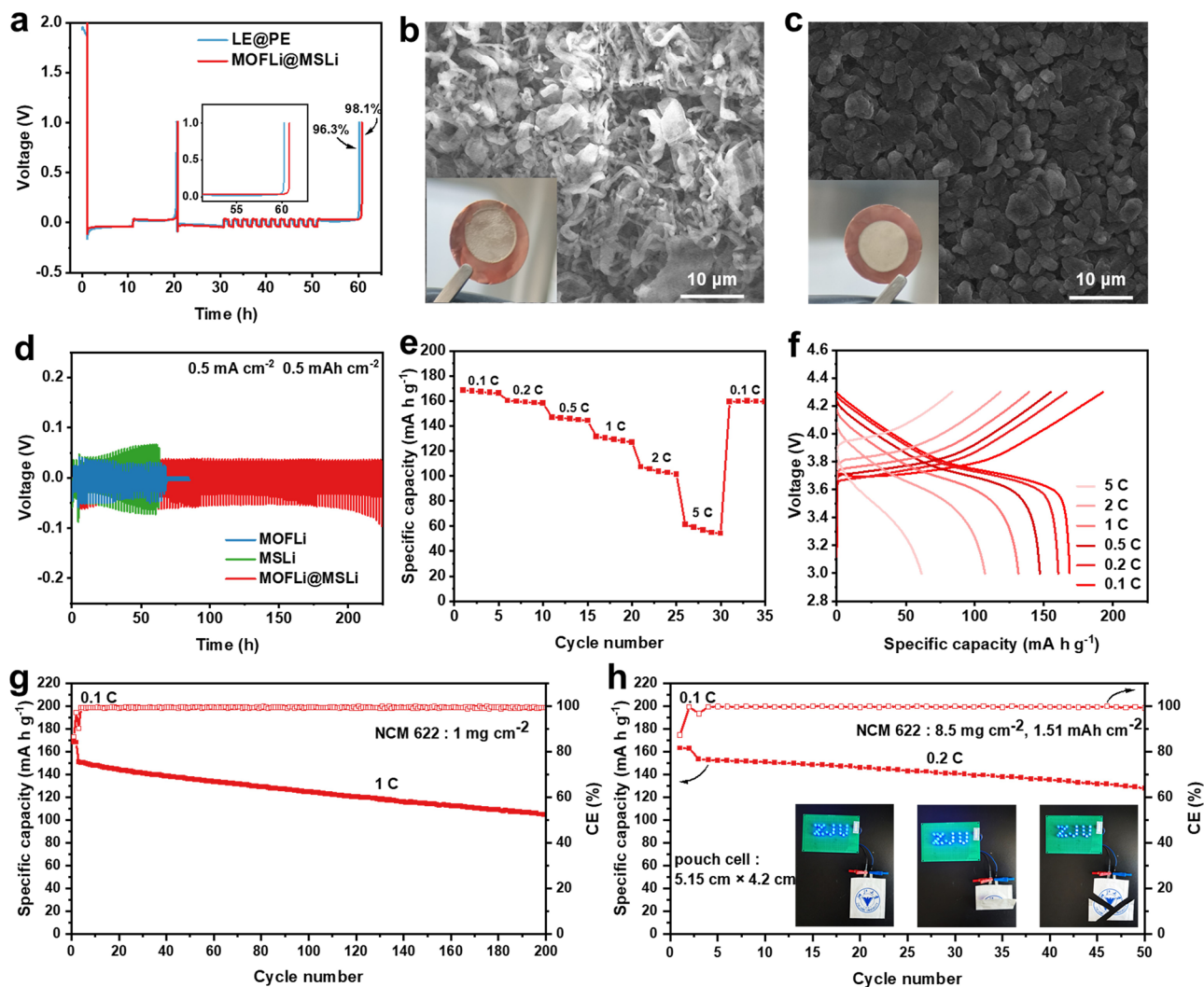


Fig. 4 Half cells and full batteries performance. **a** Average CE of LillCu cells using PE membrane and MOFLi/MSLi QSEs at a current density of 0.5 mA cm⁻². The morphology of the deposited Li with a depositing capacity of 2 mAh cm⁻² on Cu when using **b** PE membrane and **c** MOFLi/MSLi QSEs. The inset images were the optical picture of the deposited Li. **d** Cycle performance of Lillthin Li symmetric cells at a current density of 0.5 mA cm⁻². **e–f** Rate performance of NCM 622/MOFLi/MSLiLi batteries and the corresponding voltage profile. **g** Cycling performance of NCM 622//Li batteries at 1 C. **h** Cycling performance of pouch cell with high mass loading cathode. The inset was the safety illustration of pouch cell with MOF/MS electrolyte under abuse use

capacity retention. Large-size pouch cell (5.15 cm × 4.2 cm) with high mass loading cathode (8.5 mg cm⁻², 1.51 mAh cm⁻¹) could also stable work at 0.2 C. Benefiting the solid-like nature of MOFLi/MSLi QSEs and confinement of liquid electrolyte in nanopores, pouch cell showed excellent safety and high tolerance toward abused uses such as bending and cutting (Fig. 4h).

4 Conclusion

In this work, we present a Janus MOFLi/MSLi QSEs with asymmetric porous structure for LMBs. The Janus electrolyte was found to inherit the advantages of mesoporous MS and microporous MOF, maintaining both high σ_{Li+} of 1.5×10^{-4} S cm⁻¹ and high t_+ of 0.71. MD simulations revealed a concentrated-electrolyte-like solvation structure

and preferred distribution of Li^+ near the Lewis-base O atoms in the nanoporous channels, as well as regulated ion transport dynamics. Meanwhile, the nanoporous structure would homogenize the Li deposition by regulating the ion flux. As a result, Li||Cu cells equipped with the Janus MOFLi/MSLi QSEs delivered a high CE of 98.1%, compared with 96.3% when using PE membrane. NCM 622||Li quasi-solid batteries assembled with MOFLi/MSLi QSEs showed promising rate performance and stably worked for 200 cycles at 1 C. This work demonstrates how to regulate the solvation structure and ion transport by proper pore structure design for QSEs, which enables highly selective Li^+ ion conduction with high conductivity.

Acknowledgements This work is supported by National Natural Science Foundation of China (Grant No. 22005266), Zhejiang Provincial Natural Science Foundation (Grant No. LR21E020003), and “the Fundamental Research Funds for the Central Universities” (2021FZZX001-09). The authors would like to thank Shiyanjia Lab (www.shiyanjia.com) for the Raman and contact angle analysis, eceshi (www.eceshi.com) for XPS test, and Shan Yang from School of Materials Science and Engineering, Zhejiang University, for AFM test.

Declarations

Conflict of interest There are no conflicts to declare. All authors have no known competing financial interests or personal relationships that could have appeared to influence the work reported in this paper.

Open Access This article is licensed under a Creative Commons Attribution 4.0 International License, which permits use, sharing, adaptation, distribution and reproduction in any medium or format, as long as you give appropriate credit to the original author(s) and the source, provide a link to the Creative Commons licence, and indicate if changes were made. The images or other third party material in this article are included in the article’s Creative Commons licence, unless indicated otherwise in a credit line to the material. If material is not included in the article’s Creative Commons licence and your intended use is not permitted by statutory regulation or exceeds the permitted use, you will need to obtain permission directly from the copyright holder. To view a copy of this licence, visit <http://creativecommons.org/licenses/by/4.0/>.

Supplementary Information The online version contains supplementary material available at <https://doi.org/10.1007/s40820-024-01325-4>.

References

1. H. Furukawa, K.E. Cordova, M. O’Keeffe, O.M. Yaghi, The chemistry and applications of metal–organic frameworks. *Science* **341**, 1230444 (2013). <https://doi.org/10.1126/science.1230444>
2. J.L.C. Rowsell, O.M. Yaghi, Metal–organic frameworks: a new class of porous materials. *Microporous Mesoporous Mater.* **73**, 3–14 (2004). <https://doi.org/10.1016/j.micromeso.2004.03.034>
3. S.-Y. Ding, W. Wang, Covalent organic frameworks (COFs): from design to applications. *Chem. Soc. Rev.* **42**, 548–568 (2013). <https://doi.org/10.1039/C2CS35072F>
4. X. Feng, X. Ding, D. Jiang, Covalent organic frameworks. *Chem. Soc. Rev.* **41**, 6010–6022 (2012). <https://doi.org/10.1039/c2cs35157a>
5. K. Geng, T. He, R. Liu, S. Dalapati, K.T. Tan et al., Covalent organic frameworks: design, synthesis, and functions. *Chem. Rev.* **120**, 8814–8933 (2020). <https://doi.org/10.1021/acs.chemrev.9b00550>
6. U. Olsbye, S. Svelle, M. Bjørgen, P. Beato, T.V. Janssens et al., Conversion of methanol to hydrocarbons: How zeolite cavity and pore size controls product selectivity. *Angew. Chem. Int. Ed.* **51**, 5810–5831 (2012). <https://doi.org/10.1002/anie.201103657>
7. Z. Chang, H. Yang, X. Zhu, P. He, H. Zhou, A stable quasi-solid electrolyte improves the safe operation of highly efficient lithium-metal pouch cells in harsh environments. *Nat. Commun.* **13**, 1510 (2022). <https://doi.org/10.1038/s41467-022-29118-6>
8. L. Shen, H.B. Wu, F. Liu, J.L. Brosmer, G. Shen et al., Creating lithium-ion electrolytes with biomimetic ionic channels in metal-organic frameworks. *Adv. Mater.* **30**, e1707476 (2018). <https://doi.org/10.1002/adma.201707476>
9. B.M. Wiers, M.-L. Foo, N.P. Balsara, J.R. Long, A solid lithium electrolyte via addition of lithium isopropoxide to a metal–organic framework with open metal sites. *J. Am. Chem. Soc.* **133**, 14522–14525 (2011). <https://doi.org/10.1021/ja205827z>
10. S. Bai, X. Liu, K. Zhu, S. Wu, H. Zhou, Metal–organic framework-based separator for lithium–sulfur batteries. *Nat. Energy* **1**, 16094 (2016). <https://doi.org/10.1038/nenergy.2016.94>
11. H. Chen, H. Tu, C. Hu, Y. Liu, D. Dong et al., Cationic covalent organic framework nanosheets for fast Li-ion conduction. *J. Am. Chem. Soc.* **140**, 896–899 (2018). <https://doi.org/10.1021/jacs.7b12292>
12. X. Li, Q. Hou, W. Huang, H.-S. Xu, X. Wang et al., Solution-processable covalent organic framework electrolytes for all-solid-state Li–organic batteries. *ACS Energy Lett.* **5**, 3498–3506 (2020). <https://doi.org/10.1021/acsenenergylett.0c01889>
13. X. Chi, M. Li, J. Di, P. Bai, L. Song et al., A highly stable and flexible zeolite electrolyte solid-state Li-air battery. *Nature* **592**, 551–557 (2021). <https://doi.org/10.1038/s41586-021-03410-9>
14. Y. Xu, L. Gao, Q. Liu, Q. Liu, Z. Chen et al., Segmental molecular dynamics boosts Li-ion conduction in metal-organic

- solid electrolytes for Li-metal batteries. *Energy Storage Mater.* **54**, 854–862 (2023). <https://doi.org/10.1016/j.ensm.2022.11.029>
15. H. Yang, B. Liu, J. Bright, S. Kasani, J. Yang et al., A single-ion conducting UiO-66 metal–organic framework electrolyte for all-solid-state lithium batteries. *ACS Appl. Energy Mater.* **3**, 4007–4013 (2020). <https://doi.org/10.1021/acsaem.0c00410>
 16. F. Zhu, H. Bao, X. Wu, Y. Tao, C. Qin et al., High-performance metal-organic framework-based single ion conducting solid-state electrolytes for low-temperature lithium metal batteries. *ACS Appl. Mater. Interfaces* **11**, 43206–43213 (2019). <https://doi.org/10.1021/acsaami.9b15374>
 17. Z. Chang, Y. Qiao, H. Deng, H. Yang, P. He et al., A liquid electrolyte with de-solvated lithium ions for lithium-metal battery. *Joule* **4**, 1776–1789 (2020). <https://doi.org/10.1016/j.joule.2020.06.011>
 18. Z. Chang, Y. Qiao, H. Yang, X. Cao, X. Zhu et al., Sustainable lithium-metal battery achieved by a safe electrolyte based on recyclable and low-cost molecular sieve. *Angew. Chem. Int. Ed.* **60**, 15572–15581 (2021). <https://doi.org/10.1002/anie.202104124>
 19. Z. Chang, H. Yang, Y. Qiao, X. Zhu, P. He et al., Tailoring the solvation sheath of cations by constructing electrode front-faces for rechargeable batteries. *Adv. Mater.* **34**, e2201339 (2022). <https://doi.org/10.1002/adma.202201339>
 20. H.J.S. Sand III., On the concentration at the electrodes in a solution, with special reference to the liberation of hydrogen by electrolysis of a mixture of copper sulphate and sulphuric acid. *Lond. Edinb Dublin Philos. Mag. J. Sci.* **1**, 45–79 (1901). <https://doi.org/10.1080/14786440109462590>
 21. P. Dong, X. Zhang, W. Hiscox, J. Liu, J. Zamora et al., Toward high-performance metal-organic-framework-based quasi-solid-state electrolytes: tunable structures and electrochemical properties. *Adv. Mater.* **35**, e2211841 (2023). <https://doi.org/10.1002/adma.202211841>
 22. M.L. Aubrey, R. Ameloot, B.M. Wiers, J.R. Long, Metal-organic frameworks as solid magnesium electrolytes. *Energy Environ. Sci.* **7**, 667–671 (2014). <https://doi.org/10.1039/C3EE43143F>
 23. W. He, D. Li, S. Guo, Y. Xiao, W. Gong et al., Redistribution of electronic density in channels of metal–Organic frameworks for high-performance quasi-solid lithium metal batteries. *Energy Storage Mater.* **47**, 271–278 (2022). <https://doi.org/10.1016/j.ensm.2022.02.003>
 24. T. Hou, W. Xu, X. Pei, L. Jiang, O.M. Yaghi et al., Ionic conduction mechanism and design of metal-organic framework based quasi-solid-state electrolytes. *J. Am. Chem. Soc.* **144**, 13446–13450 (2022). <https://doi.org/10.1021/jacs.2c03710>
 25. Z. Miao, F. Zhang, H. Zhao, M. Du, H. Li et al., Tailoring local electrolyte solvation structure via a mesoporous molecular sieve for dendrite-free zinc batteries. *Adv. Funct. Mater.* **32**, 2111635 (2022). <https://doi.org/10.1002/adfm.202111635>
 26. L. Han, Z. Wang, D. Kong, L. Yang, K. Yang et al., An ordered mesoporous silica framework based electrolyte with nanowetted interfaces for solid-state lithium batteries. *J. Mater. Chem. A* **6**, 21280–21286 (2018). <https://doi.org/10.1039/C8TA08875F>
 27. K. Wang, C. Li, Y. Liang, T. Han, H. Huang et al., Rational construction of defects in a metal–organic framework for highly efficient adsorption and separation of dyes. *Chem. Eng. J.* **289**, 486–493 (2016). <https://doi.org/10.1016/j.cej.2016.01.019>
 28. Z. Li, Q. Liu, L. Gao, Y. Xu, X. Kong et al., Quasi-solid electrolyte membranes with percolated metal–organic frameworks for practical lithium-metal batteries. *J. Energy Chem.* **52**, 354–360 (2021). <https://doi.org/10.1016/j.jechem.2020.04.013>
 29. Y. Xu, L. Gao, L. Shen, Q. Liu, Y. Zhu et al., Ion-transport-rectifying layer enables Li-metal batteries with high energy density. *Matter* **3**, 1685–1700 (2020). <https://doi.org/10.1016/j.matt.2020.08.011>
 30. G. Wang, J. Gao, Y. Fu, Z. Ren, J. Huang et al., Implantable composite fibres with Self-supplied H₂O₂ for localized chemodynamic therapy. *Chem. Eng. J.* **388**, 124211 (2020). <https://doi.org/10.1016/j.cej.2020.124211>
 31. L. Valenzano, B. Civalieri, S. Chavan, S. Bordiga, M.H. Nilsen et al., Disclosing the complex structure of UiO-66 metal organic framework: a synergic combination of experiment and theory. *Chem. Mater.* **23**, 1700–1718 (2011). <https://doi.org/10.1021/cm1022882>
 32. G.C. Shearer, S. Chavan, S. Bordiga, S. Svelle, U. Olsbye et al., Defect engineering: tuning the porosity and composition of the metal–organic framework UiO-66 via modulated synthesis. *Chem. Mater.* **28**, 3749–3761 (2016). <https://doi.org/10.1021/acs.chemmater.6b00602>
 33. S. Mohebbi, M. Shariatipour, B. Shafie, M.M. Amini, Encapsulation of tamoxifen citrate in functionalized mesoporous silica and investigation of its release. *J. Drug Deliv. Sci. Technol.* **62**, 102406 (2021). <https://doi.org/10.1016/j.jddst.2021.102406>
 34. M. Taddei, When defects turn into virtues: the curious case of zirconium-based metal-organic frameworks. *Coord. Chem. Rev.* **343**, 1–24 (2017). <https://doi.org/10.1016/j.ccr.2017.04.010>
 35. L. Cai, H. Ying, P. Huang, Z. Zhang, H. Tan et al., In-situ grown Ti₃C₂T@CoSe₂ heterostructure as trapping-electrocatalyst for accelerating polysulfides conversion in lithium-sulfur battery. *Chem. Eng. J.* **474**, 145862 (2023). <https://doi.org/10.1016/j.cej.2023.145862>
 36. L. Liu, Z. Chen, J. Wang, D. Zhang, Y. Zhu et al., Imaging defects and their evolution in a metal-organic framework at sub-unit-cell resolution. *Nat. Chem.* **11**, 622–628 (2019). <https://doi.org/10.1038/s41557-019-0263-4>
 37. Q. Han, L. Cai, P. Huang, S. Liu, C. He et al., Fast ionic conducting hydroxyapatite solid electrolyte interphase enables ultra-stable zinc metal anodes. *ACS Appl. Mater. Interfaces* **15**, 48316–48325 (2023). <https://doi.org/10.1021/acsaami.3c11649>
 38. Z. Wang, W. Huang, J. Hua, Y. Wang, H. Yi et al., An anionic-MOF-based bifunctional separator for regulating lithium deposition and suppressing polysulfides shuttle in Li–S batteries.



- Small Meth. **4**, 2000082 (2020). <https://doi.org/10.1002/smt.202000082>
39. Y. Sun, T. Yang, H. Ji, J. Zhou, Z. Wang et al., Boosting the optimization of lithium metal batteries by molecular dynamics simulations: a perspective. *Adv. Energy Mater.* **10**, 2002373 (2020). <https://doi.org/10.1002/aenm.202002373>
40. S. Bai, Y. Sun, J. Yi, Y. He, Y. Qiao et al., High-power Li-metal anode enabled by metal-organic framework modified electrolyte. *Joule* **2**, 2117–2132 (2018). <https://doi.org/10.1016/j.joule.2018.07.010>
41. S. Yuan, J.L. Bao, J. Wei, Y. Xia, D.G. Truhlar et al., A versatile single-ion electrolyte with a Grotthuss-like Li conduction mechanism for dendrite-free Li metal batteries. *Energy Environ. Sci.* **12**, 2741–2750 (2019). <https://doi.org/10.1039/C9EE01473J>
42. M.F. Döpke, J. Lützenkirchen, O.A. Moulτος, B. Siboulet, J.-F. Dufrêche et al., Preferential adsorption in mixed electrolytes confined by charged amorphous silica. *J. Phys. Chem. C* **123**, 16711–16720 (2019). <https://doi.org/10.1021/acs.jpcc.9b02975>
43. K. Qian, S. Seifert, R.E. Winans, T. Li, Understanding solvation behavior of the saturated electrolytes with small/wide-angle X-ray scattering and Raman spectroscopy. *Energy Fuels* **35**, 19849–19855 (2021). <https://doi.org/10.1021/acs.energyfuels.1c03328>
44. L. Cao, D. Li, T. Deng, Q. Li, C. Wang, Hydrophobic organic-electrolyte-protected zinc anodes for aqueous zinc batteries. *Angew. Chem. Int. Ed.* **59**, 19292–19296 (2020). <https://doi.org/10.1002/anie.202008634>
45. H. Gan, J. Wu, F. Zhang, R. Li, H. Liu, Uniform Zn²⁺ distribution and deposition regulated by ultrathin hydroxyl-rich silica ion sieve in zinc metal anodes. *Energy Storage Mater.* **55**, 264–271 (2023). <https://doi.org/10.1016/j.ensm.2022.11.044>
46. X.-X. Wang, X.-W. Chi, M.-L. Li, D.-H. Guan, C.-L. Miao et al., Metal–organic frameworks derived electrolytes build multiple wetting interfaces for integrated solid-state lithium–oxygen battery. *Adv. Funct. Mater.* **32**, 2113235 (2022). <https://doi.org/10.1002/adfm.202113235>
47. B.G. Lee, Y.J. Park, Enhanced electrochemical performance of lithia/Li₂RuO₃ cathode by adding tris(trimethylsilyl)borate as electrolyte additive. *Sci. Rep.* **10**, 13498 (2020). <https://doi.org/10.1038/s41598-020-70333-2>
48. H. Ma, D. Hwang, Y.J. Ahn, M.-Y. Lee, S. Kim et al., In situ interfacial tuning to obtain high-performance nickel-rich cathodes in lithium metal batteries. *ACS Appl. Mater. Interfaces* **12**, 29365–29375 (2020). <https://doi.org/10.1021/acsami.0c06830>
49. H.Q. Pham, M. Mirolo, M. Tarik, M. El Kazzi, S. Trabesinger, Multifunctional electrolyte additive for improved interfacial stability in Ni-rich layered oxide full-cells. *Energy Storage Mater.* **33**, 216–229 (2020). <https://doi.org/10.1016/j.ensm.2020.08.026>